Cathodically Deposited ZIF-8 Compact Layer on an 8-µm Ultrathin Polypropylene Separator to Enhance the Performance of Lithium-Sulfur and Lithium-Metal Batteries

Xueyan Lin[a], Rishav Baranwal[a], Guofeng Ren[b], Zhaoyang Fan[c*]

[a]School for Engineering of Matter, Transport & Energy, Arizona State University, Tempe, AZ 85281, USA

[b]Shenzhen Mosu Tech, Shenzhen, Guangdong 51800, China

[c]School of Electrical, Computer and Energy Engineering, Arizona State University, Tempe, AZ 85281, USA

*Contact: zyfan@asu.edu

Abstract

The development of high-performance battery technologies necessitates ultrathin separators with superior mechanical strength and electrochemical properties. We present an innovative 1 µm thick, pinhole-free zeolitic imidazolate framework-8 (ZIF-8) layer, cathodically deposited on an 8 µm thick commercial polypropylene (PP) film in a rapid process, resulting in a ZIF-8@8-µm PP flexible membrane. This crack-free ZIF-8 layer, featuring angstrom-scale pores and chemical polar groups, functions as a Li^+ sieve, regulating Li^+ transport, controlling Li deposition, and blocking dissolved active cathode materials. It also enhances Li^+ diffusion and transference number, extending the Sand's time for Li dendrite formation. Consequently, the ZIF-8@8-µm PP separator addresses polysulfide shuttling in Li-S batteries and Li dendrite formation in Li-metal batteries, significantly improving their performance compared to conventional separators. Our findings indicate that while the 8-µm PP alone is unsuitable as a battery separator, the ZIF-8@8-µm PP, possesses the mechanical strength and electrochemical properties necessary for developing both Li-S and Li-metal batteries, as well as application in conventional Li-ion batteries with enhanced volumetric energy densities.

Keywords: Battery separator; Flexible MOF membrane; Battery separator functionalization; Li-S battery; Li-Metal Battery

1. Introduction

Li-metal batteries (LMBs), using Li-metal as the anode, are promising for next generation energy storage due to lithium's highest specific capacity (3861 mAh g^{-1}) and lowest negative potential (-3.04 V vs. standard hydrogen electrode) [1]. Taking a further step, by using sulfur as the cathode, lithium-sulfur batteries (LSBs) have garnered significant attention among LMBs. The sulfur cathode offers a superior theoretical specific capacity of 1672 mAh g^{-1}, along with the merits of environmental friendliness and abundance of sulfur, potentially overcoming the limitations of lithium-ion batteries [2,3].

The practical implementation of LMBs is hindered by the uncontrolled lithium dendrite formation on the metallic lithium anode during cycling. Moreover, the growth of lithium dendrites exposes fresh lithium to the electrolyte, leading to their continuous reaction, which results in rapid capacity degradation, low Coulombic efficiency and electrolyte consumption[4]. LSBs inherit the Li dendrites and other Li-metal problems of LMBs. Additionally, they face challenges associated with the sulfur cathode, among which the notorious 'shuttle effect' is a major technical issue. This effect is caused by the dissolution and migration of intermediate lithium polysulfides (LiPSs) to the anode, giving rise to the subsequent reactions[5] with serious consequences[6], particularly an irreversible capacity loss.

The fundamental function of the separator in a battery is to isolate the active cathode materials from those of the anode while providing pathways for rapid electrolytic Li^+ transport. Polyolefin-based membranes, including polypropylene (PP) and polyethylene (PE), characterized by large (up to hundreds of nanometers) and non-uniform micropores, are commonly used as battery separators. However, these polyolefin separators cannot fulfill their two fundamental roles since they can neither block polysulfide crossover nor facilitate Li^+ transportation. While significant

research efforts have been dedicated to immobilizing polysulfides within the cathode host[7-9], achieving effective separation using the separator remains a solution to polysulfide shuttling. With a nonpolar surface property, these separator materials are not able to expedite Li^+ transportation.

The formation of lithium dendrites can be modeled by Sand's time (or capacity) [10], which suggests that to prevent dendrite formation, the diffusion (D_+) and transference number (t_+) of Li^+ in electrolyte should be maximized, while its flux (J) should be minimized. Polyolefin-based "passive" separators lack functional groups that actively regulate ion transport to enhance Li^+ diffusion and its transference number. On the other hand, the random pore size and pore distribution in these passive separators leads to an inhomogeneous Li^+ flux[11], increasing localized Li^+ flux. These separators not only fail to effectively separate the active electrode materials and promote Li^+ transportation but also exacerbate the dendrite problem. Modifying the separator by reducing pore size or functionalizing it to facilitate uniform and rapid Li^+ transfer and block polysulfide pathway emerges as a promising approach to mitigate the lithium dendrite problem and the shuttle effect in LMBs and LSBs[12].

Even though being an indispensable component of batteries, the passive separator itself does not actively contribute to any battery capacity, while with a typical thickness of 20-30 μm, it occupies a significant portion of the battery volume [13]. Reduction of separator thickness can help increase the battery volumetric energy density[14]. For instance, replacing the 30 μm thick separator with 10 μm ultrathin one, NCM811-based LIB will increase its energy density from 700 to 820 Wh L^{-1}. Reduction of internal resistance is another merit of ultrathin separators. Yet, these ultrathin PP or PE separators lack the necessary puncture strength and mix penetration resistance that are crucial for battery manufacturing[15]. Moreover, they do not possess enough mechanical

strength to endure the long-term battery cycling [14]. They certainly cannot prevent Li dendrite penetration if a metal Li anode is used.

Therefore, it becomes an urgent subject to engineer an ultrathin separator with active functions to help solve the challenges of polysulfide shuttling and Li dendrite formation, while possessing enough mechanical strength to endure long-term battery cycling and maintaining high volumetric energy density. Indeed, considerable works have been done in developing new polymer separators that prevent lithium dendrite formation and polysulfide shuttling in LSBs. Separators have been coated or functionalized with various polar groups to create a physical and chemical barrier[16-19]. However, these coatings lack the appropriate physical and chemical pore structure, making them less effective. Additionally, the resulted separators are typically not in the ultrathin rage (< 10 μm).

In this context, metal-organic frameworks (MOFs), coordinated by metallic nodes and organic ligands, known for their highly ordered and tunable pore size structures, might provide a solution[20]. MOFs possess precisely controllable sub-nanoscale structures that can accommodate liquid electrolytes, serve as ion/molecule sieves to block polysulfide crossing over and regulate/enhance Li^+ transportation, and homogenize Li^+ flux on the Li-metal surface, thus help addressing the two challenges of Li dendritic growth and polysulfide shuttling [21-23]. Indeed, various MOFs have been explored for these purposes for LMBs and LSBs. For instance, UIO-66, a Zr-based MOF with open metal sites, attracts and immobilizes anions, increasing t_{Li+} from 0.49 to 0.79 and σ_{Li+} from 0.3 to 1.7 mS cm^{-1}.[24] Amine group functionalized NH_2-MIL-125(Ti) accelerates cation transport and retards anion diffusion, thus increasing t_{Li+} to 0.78 [25]. Thick ZIF-67 powder coated LIB separator [26] was demonstrated to immobilize PF_6^- and dramatically increase t_{Li+} to 0.81 and σ > 1.5 mS cm^{-1}. MOFs@GO as separators of LSBs displayed a low-

capacity decay rate of 0.041% per cycle at 1C [27].

In the broad field of MOF-based membrane technology, although many synthesis techniques have been developed, preparing uniform and crack-free MOF layers with a sub-μm thickness on flexible porous substrates has remained a challenge[28,29]. The tens of micrometers thick MOF powder coating is excluded. Techniques such as layer-by-layer assembly and phase transformation interfacial growth could fulfill this purpose, but they usually need tens of hours for deposition, and hence are not suitable for large-scale battery separator applications. In this regard, cathodic (electro)deposition method provides a new opportunity for fabricating crack-free MOF films with shorter synthesis time and thickness/morphology controlled[30,31].

Among a variety of MOFs, ZIF-8 (Zeolitic Imidazolate Frameworks-8) stands out attributed to its suitable pore size and high thermal and chemical stability[32-37]. Herein, we employed an aqueous cathodic deposition method[30,38-41] to in-situ grow a pinhole-free and crack-free ZIF-8 compact thin film with a sub-μm thickness on both conventional (25 μm) and ultrathin (8 μm) PP membranes[28,42] used as separators in LSBs and LMBs. The ZIF-8 modification not only facilitates the electrolyte affinity but also serves as an ion/molecule sieve to facilitate and regulate Li^+ transportation as well as inhibit soluble polysulfide shuttling. In addition, the modified ultrathin ZIF-8@8-μm PP separators overcome the mechanical and electrochemical limitations of pristine 8-μm PP separators while maintaining their merits of lower internal resistance and higher ionic conductance due to the shortened distance. Therefore, the use of the ZIF-8@PP separator in Li||Li symmetric and Li||Cu asymmetric cells for Li stripping/plating studies demonstrated smaller polarization voltage, higher coulombic efficiency, and significantly enhanced lithium stripping/plating cycling stability compared to cells utilizing pristine PP separators. Consequently, LSBs equipped with the ZIF-8@8-μm PP separator delivered a high initial capacity of 1480 mAh

120 g^{-1} as well as a low capacity-degradation rate of 0.031% per cycle at 1C within 500 cycles.
121 Similarly, LMBs (Li||LiFePO4) coupled with the ZIF-8@8-μm PP also demonstrated
122 substantially enhanced performance.

123 ## 2. Results and Discussion

124 ### 2.1. Cathodic deposition of ZIF-8 films

125 Fig. 1(a) illustrates the structure and formation process of the 3-D crystal lattice of ZIF-8. The
126 lattice structure consists of a Zn(II) ion tetrahedrally coordinated with four 2-methylimidazolate
127 ligands via Zn-N bonds. When 2-methylimidazole ($C_4H_6N_2$, MIM) loses a proton, it becomes 2-
128 methylimidazolate ($C_4H_5N_2^-$, MIM^-). The deprotonated nitrogen (N^-) coordinates with a Zn^{2+} ion.
129 Additionally, the second nitrogen in the imidazolate ring, which is not deprotonated, has a lone
130 pair of electrons that can interact with another Zn^{2+} ion, though not as strongly as the negatively
131 charged nitrogen. Consequently, each of the four 2-methylimidazolate ligands, tetrahedrally
132 coordinated to a Zn(II) ion, bridges to another Zn(II) ion. This interaction forms a 3D network that
133 can be visualized as a tetrahedral coordination geometry around each zinc ion, with each 2-
134 methylimidazolate ligand bridging two zinc centers. Thus formed ZIF-8 features a pore diameter
135 of approximately 11.6 Å and a window size of 3.4 Å [43]. The inset SEM image illustrates the common
136 rhombic dodecahedral morphology of ZIF-8 particles synthesized in a hydrothermal process. ZIF-
137 8 combines the advantages of both MOFs and zeolites, exhibiting properties such as high
138 crystallinity, porosity, and remarkable chemical and thermal stability.
139
140
141
142

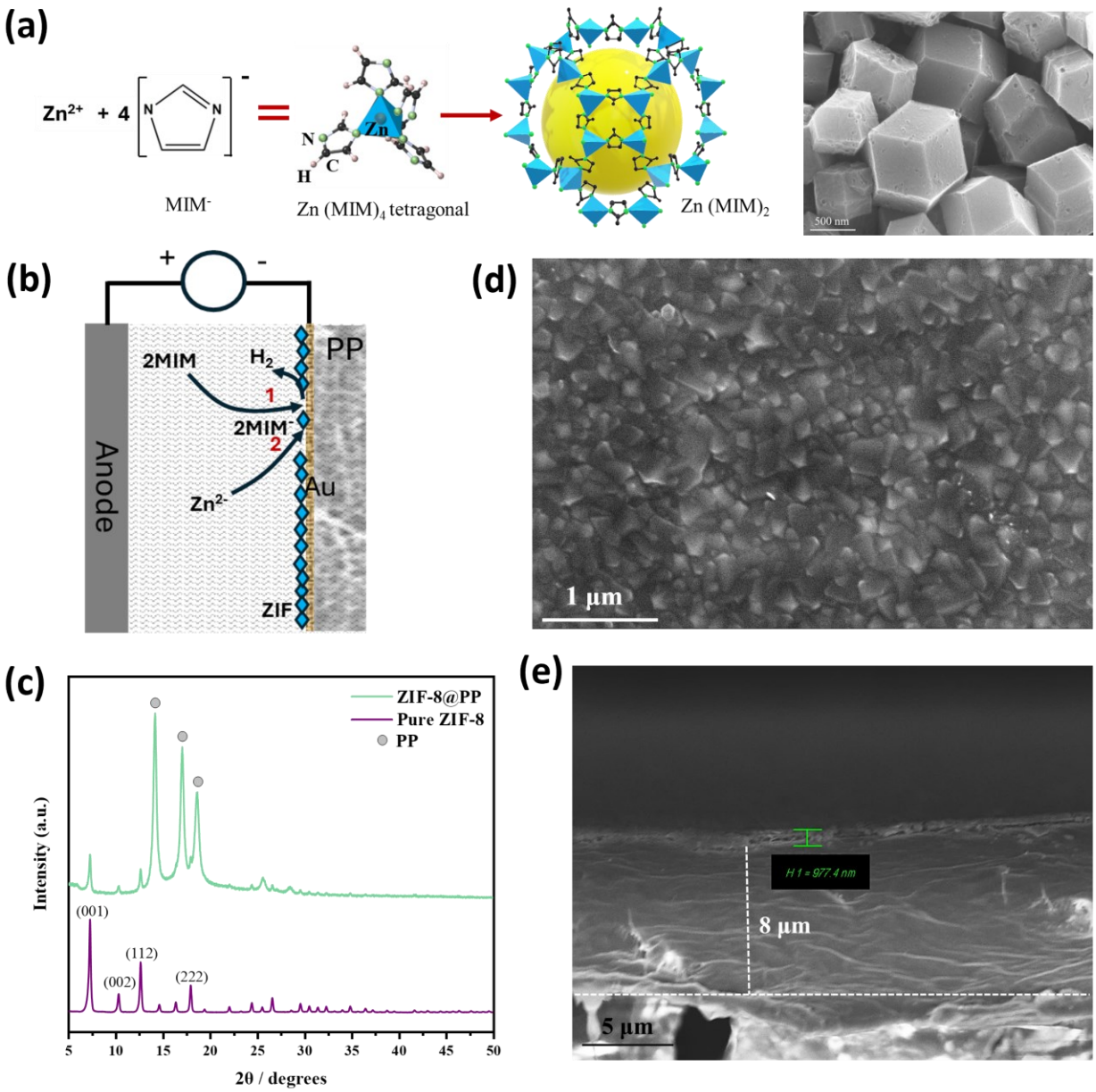

Fig. 1. (a) The scheme of the chemical reaction to synthesize ZIF-8, its porous structure, and the typical morphology of ZIF-8 crystals. (b) The electrochemical synthesis process of ZIF-8 on PP membrane. (c) XRD pattern of ZIF-8@PP and pure ZIF-8 crystals. SEM top view (d) and cross-sectional view (e) of ZIF-8@8-μm PP separator.

Fig. 1(b) shows the process of cathodic electrodeposition of ZIF-8 on a porous PP membrane. A few nanometers thick gold is first deposited on the commercial PP separator in a sputtering tool. The gold layer is used as the cathode and as the hydrogen evolution catalyst. With Au/PP as the cathode, graphite paper as the anode, and MIM and Zn salt solution as the electrolyte, a small current (0.13 mA cm^{-2}) is applied for electrodeposition. When MIM diffuses to the cathode surface, it is reduced by deprotonation: $2MIM + 2e^- = 2MIM^- + H_2$ (Reaction 1 in Fig. 1(b)). Meanwhile, Zn^{2+} in the solution migrates to the cathode, coordinating with MIM^-: $Zn^{2+} + 2MIM^- = Zn(MIM)_2$ (Reaction 2 in Fig. 1(b)), nucleating on the Au-coated PP surface, and eventually forming a film. Since ZIF-8 is electronically insulating, deprotonation of MIM more easily occurs at the spots on the cathode where ZIF-8 has no perfect coverage. Therefore, electrodeposition is a self-limiting process, which ensures complete and pinhole-free coverage of ZIF-8 on the PP separator, while its thickness is self-limited. In this work, a crack-free layer with full coverage was obtained after 1 h deposition, which was confirmed by the thin-film optical interference observed in the resultant ZIF-8@PP composite separator, as shown in Fig. S1 in the Supplementary Information (SI). Fig. S2 presents the porous morphology of the pristine PP membrane.

The XRD pattern of the ZIF-8@PP membrane, as shown in Fig. 1 (c), reveals three distinct peaks centered at the 2θ angles of 14.0°, 16.9° and 18.5°, corresponding to the (110), (040) and (130) crystallographic planes of the PP substrate, respectively [44]. Additionally, peaks at 7.3°, 10.35°, 12.7° and 18.0° emerge, attributed to the (001), (002), (112), and (222) planes of ZIF-8 crystals. This observation suggests the successful deposition of ZIF-8 film[45,46]. By using the PP membrane substrate with different thickness (8 μm vs. 25 μm), the resultant ZIF-8 deposited PP membranes were denoted as ZIF-8@8-μm PP and ZIF-8@25-μm PP, respectively. SEM images

in Fig.1 (d) (top view) and Fig. S4 (tilted view) reveal the surface morphology of the ZIF-8 film on a PP membrane, demonstrating the formation of a crack-free and uniform layer of ZIF-8 crystals on the surface of 8 μm thick PP membrane. Similarly, a compact ZIF-8 layer was also deposited on 25 μm thick PP membrane, as observed from Fig. S5.

2.2. Characteristics of ZIF-8@PP separator

The X-ray photoelectron spectroscopy (XPS) analysis was carried out to study the chemical composition of the materials. As depicted in the wide XPS surveys (Fig. S6(a)), Zn 2p, N 1s and O 1s peaks emerge in ZIF-8@PP samples after cathodic deposition. In the Zn 2p spectra of ZIF-8@PP (Fig. S6(b)), two narrow peaks are evident, corresponding to Zn 2p3/2 at 1022.2 eV and Zn 2p1/2 at 1045.1 eV, respectively. This observation suggests that the majority of zinc ions are in tetrahedral coordination[47]. The N 1s spectra of the ZIF-8@PP sample in Fig. S6(c) exhibits two peaks at 400 and 398.9 eV, attributed to the C=N and C-N bonds, respectively, in the 2-methylimidazole organic ligands [48]. This observation is consistent with the C-N signal detected in the C 1s spectra of ZIF-8@PP, whereas pristine PP only contains C-C bonds without additional polar functional groups (Fig. S6(d))[49,50].

The elemental configuration of the four studied separators was further investigated using Fourier-transform infrared (FT-IR) spectrometer. In Fig. 2(a), the spectrum of the pristine PP is similar to the one observed in previous studies [51], while the change in intensity peaks of the modified separators is evident, indicating the presence of additional functional groups introduced by the very thin ZIF-8 layer. The additional C-H bending observed in the wavelength region of 2800-3000 cm^{-1} in the ZIF-modified separator indicates the presence of methyl groups from the ZIF-8 rings. The nitrogen-coordinated zinc atoms are confirmed by Zn-N vibrations at approximately 421 cm^{-1}. Furthermore, the C-N and C=N vibrations at approximately 1150 cm^{-1}

and 1585 cm^{-1}, respectively, confirm the formation of functional groups due to ZIF-8 deposition [52].

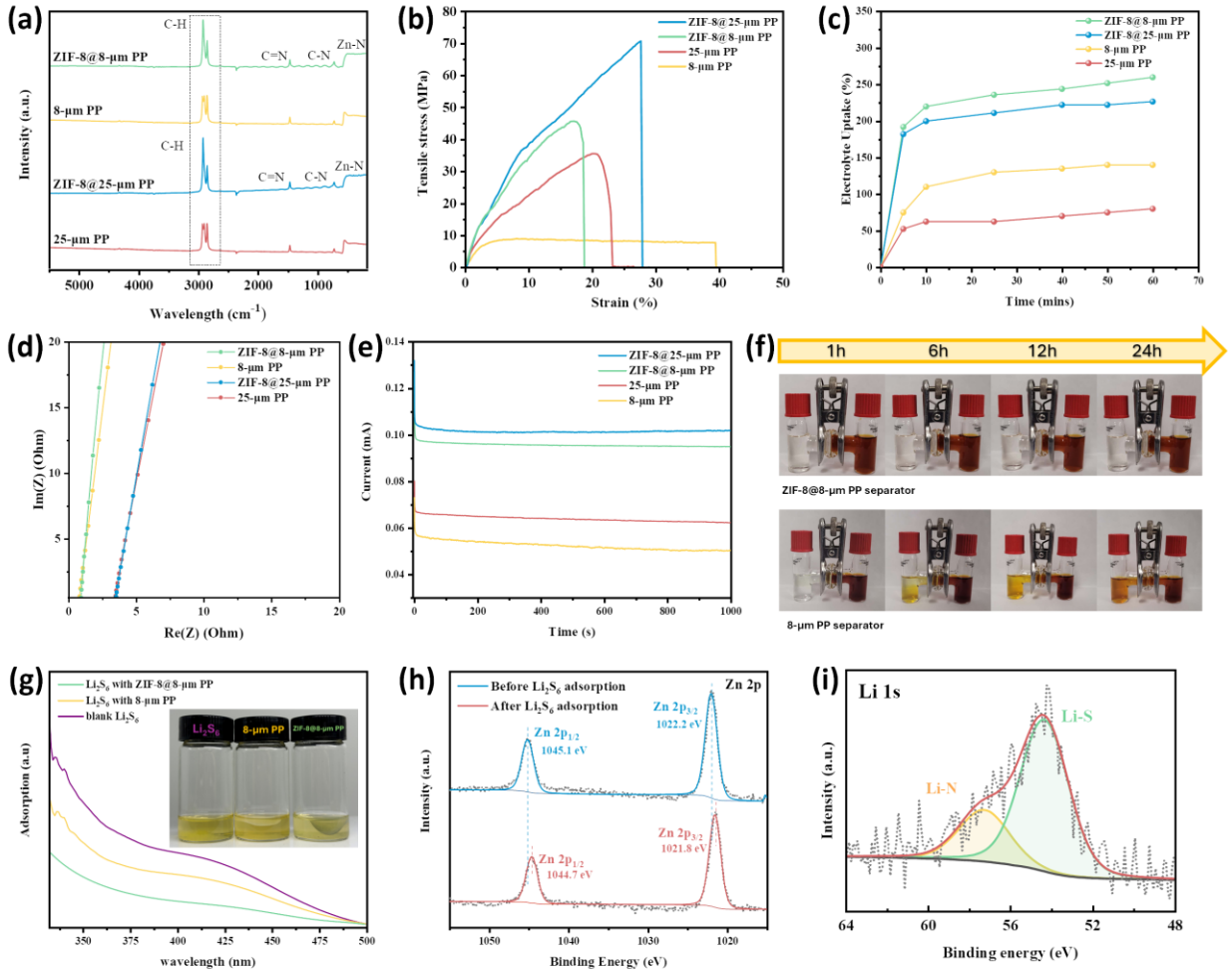

Figure 2. (a) FT-IR spectra of four different separators. (b) Stress-strain characteristics of different separators under uniaxial elongation. (c) Electrolyte uptake demonstration of different separators. (d) The EIS profiles of two-electrode symmetrical stainless-steel cells coupled with different separators. (e) The chronoamperometry profiles of two-electrode symmetrical lithium metal cells coupled with different separators. (f) Polysulfide permeation tests in H-type cell through ZIF-8@8-μm PP and commercial 8-μm PP membranes. (g) UV-Vis absorbance spectra and digital photographs(inset) of 5mM Li_2S_6 solutions and Li_2S_6 solutions after interacting with

ZIF-8@8-μm PP and 8-μm PP. (h) Zn 2p XPS spectra of ZIF-8@8-μm PP before and after Li_2S_6 adsorption test. (i) Li 1s XPS spectrum of ZIF-8@8-μm PP after Li_2S_6 adsorption test.

The synthesis of continuous MOF membranes with high flexibility is practically useful and has been considered technically challenging [28]. As shown in Fig. S7, the ZIF-8@8-μm PP ultrathin separator exhibits excellent flexibility. Even after multiple times of folding and unfolding, the in-situ formed ZIF-8 layer remained firmly affixed to the surface of the ultrathin PP separator without any obvious visual changes in the thin-film optical interference, indicating the exceptional flexibility of the ZIF-8@8-μm PP separator. The mass loading of ZIF-8 on 8-μm and 25-μm PP separators was determined to be 0.04 mg/cm², with weight percentages of 6.7% and 2.6% for ZIF-8@8-μm PP and ZIF-8@25-μm PP, respectively. These values were obtained by measuring the membrane weights after each synthesis step, with areal densities summarized in Tables S1 and S2. The lightweight ZIF-8 layer ensures minimal impact on the separator's overall weight, preserving the high energy density of LSBs.

Furthermore, as illustrated in Fig. 2(b), the ZIF-8@8-μm separator demonstrated a significantly higher yield stress of approximately 45.7 MPa at a strain of 17.2%, in contrast to the pristine 8-μm PP, which exhibited a yield stress of 7.75 MPa at a strain of 39.4%. The conventional 25-μm PP separator showed a yield stress of 35.5 MPa at a strain of 20.8%, while the ZIF-8 coating increased the yield stress to 70.5 MPa at a strain of 27.8%. These results indicate that a thin ZIF-8 coating can dramatically increase the yield stress of PP separators, enabling them with superior breaking strength. This is particularly true for the fragile 8-μm PP. The tensile test confirms that the incorporation of a thin crystalline ZIF-8 layer enhances the mechanical strength, thereby overcoming the limitations of the pristine 8-μm PP.

Thermal stability is a critical factor that significantly impacts the safety and reliability of lithium-based batteries. To quantitatively characterize the thermal stability and phase changes at elevated temperatures, differential scanning calorimetry (DSC) analysis was performed (Fig. S8(a)). The pristine commercial PP separator shows a main endothermic peak at ~ 160 °C, which is close to the melting point of polypropylene [53]. However, ZIF-8 modified PP membranes shift to a higher phase transition temperature with the same substrate materials. The wider temperature window indicates the improved thermal stability of ZIF-8@PP separators. The thermal shrinkage tests shown in Fig. S8(b) were performed by keeping different separators in a drying oven and the temperature was increased up to 150°C at 5°C/min. All separators made of polypropylene material decomposed at 150°C, consistent with the DSC measurements. However, in the case of the decomposition of ZIF-8@PP separators, a coarse layer of ZIF-8 remained behind compared to pristine PP separators.

The separator, along with the electrolyte it holds, forms ionic pathways for lithium ions, aiding their transport across electrodes. Maximizing transport efficiency can be achieved by increasing the electrolyte load on separators. Fig. 2(c) presents the electrolyte uptake by different separators, with the ZIF-8 coating demonstrating higher electrolyte absorption. The lithophilic functional groups (-N, =N, -Zn-N) [20] and the cage-like porous structure of ZIF-8 enable these separators to hold a considerable amount of electrolyte, thereby enhancing electrolyte uptake. Table S3 summarizes the electrolyte uptake weight percentages of different separators.

The wettability of separators also plays a critical role in batteries, as it influences the ion transportation. A wetting test was performed by adding a droplet of the electrolyte onto the surface of each separator and observing the spread of the electrolyte over time, as shown in Fig. S9. When a droplet of electrolyte is placed on the surface of the ZIF-8@8-μm and ZIF-8@25-μm

PP separators, it rapidly spreads over and is absorbed, leading to complete wetting within 10 s. The affinity between the separator and electrolyte is closely associated with ionic conductivity and internal resistance. Efficient wetting not only improves the performance of the battery by enhancing ion transportation but also reduces the time required for electrolyte filling, simplifying manufacturing processes and extending the battery life cycle. In contrast, the commercial PP separator exhibits considerably less wetting under the same testing conditions, with the electrolyte drop observed to remain on the surface. Therefore, with the introduction of ZIF-8 thin film, fast and uniform wetting of the liquid electrolyte over the entire separator can be realized.

Unlike ceramic-coated separators containing low-surface-area ceramic particles or polymer materials with low Li^+ conductivity, the crack-free ZIF-8 layer offers a higher surface area and abundant open metal sites with an appropriate pore size. This enables efficient Li^+ transport with high Li^+ transference number. The modification of the ZIF-8 layer allows for rapid absorption of sufficient liquid electrolyte and retention of the absorbed electrolyte throughout the discharge and charge processes. This results in lower internal resistance of both separators and batteries, contributing to excellent electrochemical performance over an extended period. Consequently, the rate capability and cycle durability of the batteries are improved. In general, achieving high ionic conductivity in separators depends on having a sufficient number of pores with appropriate sizes. Additionally, good wettability with the liquid electrolyte is essential for the ionic conductivity of separators. The electrochemical impedance spectroscopy (EIS) results in Fig. 2(d) indicate that cells using the ZIF-8@8-μm and 8-μm PP separators exhibit smaller internal resistance. This lower internal resistance with the thin separator compared to the thick separator is due to reduced tortuosity for Li^+ transportation. Based on the Nyquist plots of their EIS spectra, the resistance (R) is defined at the intersection of the spectrum curve with the Zre-axis. This

resistance is used to calculate Li^+ conductivity based on the formula $\sigma = \frac{L}{RA}$, where L is the thickness and A is the area of the separator [54]. The thickness of the ZIF-8 layer has been confirmed to be approximately 1 μm. Therefore, the ZIF-8@8-μm separator with electrolyte saturated was determined to have the highest Li^+ conductivity of 0.322 mS/cm, compared to 0.307 mS/cm for the 8-μm PP separator, 0.235 mS/cm for the ZIF-8@25-μm PP separator, and 0.229 mS/cm for the 25-μm PP separator. Thus, the ZIF-8 modified separators prompt more effective ionic transport compared to the pristine PP separator due to the improved wettability, despite slightly higher membrane thicknesses.

The Li^+ transference number (t_{Li+}) is another significant factor affecting the batteries performance. To obtain the transference number of a separator, it is sandwiched between two lithium chips, and a DC potential of 10 mV is applied for 1000 sec to record the chronoamperometry, as presented in Fig. 2(e). The transference number can be calculated by $t_{Li+} = \frac{I_s(V - I_o R_o)}{I_o(V - I_s R_s)}$, where V represents the applied DC voltage (10 mV), I_o and I_s denote the initial and steady-state currents, respectively, which can be read from the chronoamperometry curves. R_o and R_s stand for the interfacial resistances before and after DC polarization, respectively, and can be derived from the EIS curves as depicted in Fig. S10[55]. With a thin ZIF-8 coating, the 25-μm PP increases its transference number from 0.61 to 0.68, while the 8-μm PP increases its value from 0.59 to 0.67. The crack-free ZIF-8 thin film enhances the permselectivity of Li^+ through the separator, resulting in an increased transference number.

Lithium polysulfides (LiPSs) are reported to easily dissolve within the commonly used ether-based electrolyte[56], and the size of desolvated and solvated LiPSs molecules is about 7 and 10-13 Å[57], which are significantly smaller than the 50-200 nm strip-shaped pores in commonly used

297 PP separators (Fig. S2). Therefore, LiPSs can easily permeate across the separator and shuttle
298 between the electrodes. The densely covered ZIF-8 layer consists of ZIF-8 nano crystals
299 possessing a small pore aperture of 3.4 Å[43], which can serve as a molecule sieve and physically
300 block the diffusion of LiPSs through the separator.

301 Previous studies have shown that MOF materials exhibit a strong Lewis acid–base interaction
302 with LiPSs [58]. In the case of ZIF-8, the Zn metal acts as a Lewis acid center, effectively trapping
303 polysulfides in the pores of ZIF-8 through strong interactions with the polysulfide soft Lewis
304 base. This interaction plays a crucial role in anchoring sulfur[27]. Additionally, the N-rich
305 functional groups present in ZIF-8 facilitate the trapping of LiPSs by forming Li-N bonds[59].
306 Therefore, besides physically inhibiting polysulfide shuttling through sub-nanoscale pore
307 apertures, the ZIF-8 modification layer can also capture and confine LiPSs by chemical
308 interactions.

309 The superior polysulfide blocking capability of the ZIF-8@8-μm PP membrane compared with
310 the pristine 8-μm PP separator can be directly observed in lithium polysulfide permeation tests.
311 As shown in Fig. 2(f), initially, the H-type cells were coupled with ZIF-8@8-μm PP and 8-μm
312 PP separator. The left tube was filled with a pure DOL/DME solution, while the right tube
313 contained a 0.025 M Li_2S_6 DOL/DME brownish solution. Over time, polysulfide diffusion from
314 right to left became evident with the 8-μm PP separators, noticeable after 24 hours. In contrast,
315 the ZIF-8@8-μm PP separator effectively prevented almost any Li_2S_6 from passing through
316 within the same period. Similarly, the ZIF-8@25-μm PP also strongly inhibits the polysulfide
317 shuttling compared to the pristine 25-μm PP separators as shown in Fig. S11. Based on the visual
318 observations, the permeation rate of polysulfide in 8-μm PP is slightly faster than that of 25-μm
319 PP due to the reduced diffusion distance across the separator. However, the ZIF-8@8-μm PP can

block the polysulfide shuttling as the ZIF-8@25-μm PP, which highlights the benefits of ZIF-8 modification thin film on an ultrathin PP separator.

The superior performance of crack-free ZIF-8 thin coating on inhibiting polysulfide shuttling is ascribed to its sub-nanoscale permselective pores. Each unit cell of ZIF-8 contains a micropore with a diameter of ~11.6 Å and a pore aperture of 3.4 Å. But the rotation of MIM ligands allows molecules with kinetic diameters of up to 6.7 Å to diffuse through the framework. In DOL/DME, the solvated polysulfides exist in many forms but generally have a size > 10 Å, while the solvated Li^+ and free Li^+ are only 6.4 Å and 1.8 Å, respectively [60]. Therefore, ZIF-8 can effectively block polysulfides while allowing Li^+ transport. Small de-solvated polysulfides may enter the pores, but they can be trapped there due to the presence of the MIM ligand in ZIF-8 which contains a positively charged nitrogen atom (N^+-CH_3) in the imidazole ring. This observation further implies that the ZIF-8@8-μm PP separator can function as an ionic sieve, selectively transporting Li^+ while simultaneously preventing the shuttle effects of polysulfides species.

To study the trapping effect of ZIF-8 modification layer towards LiPSs, ZIF-8@8-μm PP and pristine 8-μm PP separators were immersed in 5 mM Li_2S_6 solutions for polysulfide adsorption tests. After 12 hours of immersion, the yellow Li_2S_6 solution slightly discolored with the ZIF-8@8-μm PP separator. The changes in polysulfide concentration were quantitatively confirmed through UV-Vis absorbance spectroscopy, as shown in Fig. 2(g). A greater reduction in UV absorbance intensity was observed for ZIF-8@8-μm PP, indicating its stronger polysulfide adsorption capabilities. XPS analysis conducted before and after Li_2S_6 adsorption tests revealed the chemical interactions between ZIF-8@8-μm PP and polysulfides. As shown in the Zn 2p XPS spectra of ZIF-8@8-μm PP (Fig. 2(h)), the Zn 2p characteristic peaks shift to lower binding energies after interaction with Li_2S_6, indicating electron transfer from Li_2S_6 to the Zn sites[61].

343 Additionally, the presence of the Li 1s peak after Li_2S_6 adsorption (Fig. 2(i)) corresponds to Li-
344 S bonds at 54.6 eV and Li-N bonds at 57.2 eV, respectively[62]. In the S 2p core-level XPS spectra
345 (Fig. S12), peaks at 161.1 and 162.3 eV are attributed to terminal sulfur (S^{-1}_T) and bridging sulfur
346 (S^0_B), while the signals at 165.8 and 167.7 eV are assigned to thiosulfate and polythionate species,
347 respectively[63].

348

349 2.3. Electrochemical studies of ZIF-8@PP separators

350 The electrochemical function of ZIF-8 coating on the separator can be appreciated in the Li
351 plating/stripping test. The test was first conducted in Li||Li symmetrical cells with specific
352 capacity of 2 mAh cm^{-2} at 1 mA cm^{-2} that were assembled with different separators. The
353 electrolyte is 1 M LiTFSI in DOL/DME (1:1 vol%) with 2% $LiNO_3$.

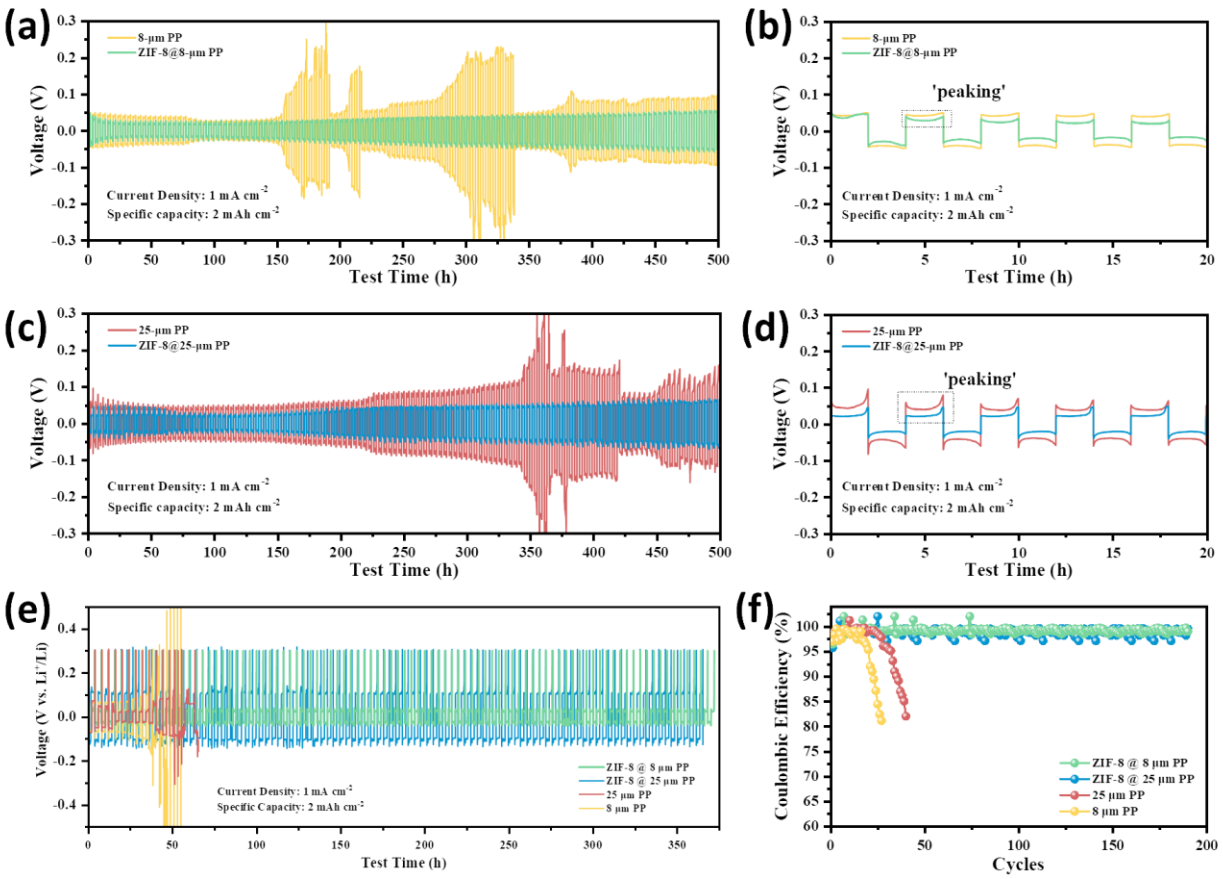

Figure 3 (a)Time–voltage curves of Li plating/stripping in Li|| 8-μm PP ||Li cell and Li|| ZIF-8@8-μm PP ||Li symmetrical cells at 1 mA cm^{-2} and 2 mAh cm^{-2} and (b) the enlarged view of time–voltage curves from 0 to 20 h. (c)Time–voltage curves of Li plating/stripping in Li|| 25-μm PP ||Li cell and Li|| ZIF-8@25-μm PP ||Li symmetrical cells at 1 mA cm^{-2} and 2 mAh cm^{-2} and (d) the enlarged view of time–voltage curves from 0 to 20 h. (e) Time-voltage curves of Li plating-stripping in Li||Cu asymmetrical cells with different separators and (f) their respective Coulombic efficiency comparison.

As shown in Fig. 3(a) and (c), the overpotential of symmetric Li||PP separator||Li metal cell gradually increases during cycling, implying a deteriorating electrode/electrolyte interface caused

by Li dendrite growth. More importantly, the cell assembled with 8-μm PP separator faced an earlier short circuit failure (~150 h) compared to 25-μm PP separator, indicating that the inherent lithium dendrites can easily penetrate through the ultrathin separator and result much faster cell failure and more severe safety hazards. However, the symmetric cells using the ZIF-8 coated separator present stable and reversible cycling with low Li stripping/plating overpotential after over 500 h in the case of both 8-μm and 25-μm separators, which obviously overcome the challenges of anode deterioration when utilizing ultrathin separator and ensure the safety for high performance LMBs. As shown in Fig. 3(b) and (d), it is noteworthy that during the initial cycles, the voltage response of Li-Li symmetric cells with different separators exhibited a characteristic 'peaking' shape, indicating spatially varying surface kinetics due to the coexistence of fast and slow interfacial reactions across the electrode surface. With extended cycling, this peaking behavior diminishes in cells with ZIF-8@PP separators, while an 'arcing' shape emerges in cells with pristine PP separators, as depicted in Fig. S13(a) and (b). The appearance of this 'arcing' behavior indicates the accumulation of dead Li, leading to large lithium-ion concentration gradients and voltage behavior dominated by mass transport limitations. As the dead Li layer grows, these mass transport constraints worsen, resulting in more pronounced arcs and increased overpotential[64]. As has been demonstrated, the compact ZIF-8 coating enhances the diffusion coefficient and transference number of Li^+. Moreover, the presence of polar functional group, open lithophilic metal sites as well as homogeneous and ordered microporous structure of ZIF-8 help to regulate the uniform deposition of lithium ions. All these contribute to the significantly expanded Sand's time and capacity before lithium dendrites appearance, thereby prolonging the lithium electrode lifespan.

Plating-stripping behavior in a Li||Cu cell was further tested to determine the Coulombic Efficiency (CE) of Li||Cu half cells with the various separators. CE hints at the reversibility of the lithium transfer in a full metal cell. These cells were tested at a large specific capacity of 4 mAh/cm^2 with a current density of 2 mA/cm^2. Fig. 3(e) shows that the plating-stripping occurs with minimum overpotential for the ZIF-8@8-μm separator. This can be attributed to improved ionic pathways with reduced length and a uniform lithium-ion flux due to the presence of a crack free uniform ZIF-8 layer. The cells with pristine separators showed signs of short circuit after ~70 and ~100 hours of cycling at this rate, while the ZIF modified separator showed almost invariable CE of ~99.5% over a course of 380 hours as evident from Fig. 3(f). This suggests that the ZIF-8@8-μm separator can inhibit the formation of lithium dendrites at a faster charging/discharging rate for a longer span compared to the other commercially available separators.

The cyclic voltammograms (CVs) obtained at scan rates of 0.2, 0.4, 0.6, 0.8, and 1 mV s^{-1} for Li-S cells coupled with different separators are illustrated in Fig. S14(a)(b) and Fig. S15 (a)(b). As the scan rate increases, the anodic peaks shift towards more positive potentials while the cathodic peaks shift towards more negative potentials, resulting in increased polarization. The CV curves exhibit a two-step redox reaction during the lithiation/delithiation of sulfur. Distinct cathodic peaks (C_1 and C_2) and one anodic peak (A) are observed in the CV curves. Cathodic peak C_1 corresponds to the reduction of sulfur (S_8) to high order polysulfides (Li_2S_8/Li_2S_4), which is equivalent to the first plateau observed in the discharge curve. Cathodic peak C_2 is attributed to the reduction of these high order polysulfides to short order polysulfides and ultimately Li_2S_2/Li_2S, corresponding to the second plateau in discharge curves. The anodic peak A represents the oxidation reaction from Li_2S_2/Li_2S back to Li_2S_8/S_8 [65]. The anodic and cathodic current peaks (I_A, I_{C1}, I_{C2}) exhibit a

linear relationship with the square root of the scanning rates (Fig. S14(c)(d) and Fig. S15(c)(d)), indicating that the ion diffusion process is the rate-determining step in the electrochemical reactions[66]. The lithium-ion diffusion coefficient (D_{Li}+) was determined using the Randles–Sevcik equation: $I_P = 2.69 \times 10^5 n^{3/2} A D^{1/2} Li C_{Li} v^{1/2}$ where I_P is the peak current, n is the number of electrons in the reaction, A is the electrode area, C_{Li} is the lithium-ion concentration in the electrolyte, and v is the scan rate[67]. The slopes can be derived from the linear relationship between the peak current I_P and $v^{1/2}$ at each redox peak. To quantitively evaluate the lithium-ion diffusion behavior coupled with different separators, the D_{Li}+ values at each redox peak were calculated and summarized in Table S4. The ZIF-8@8-μm PP exhibited the highest D_{Li}+ for each reaction step when compared to other counterparts, which suggests ZIF-8@8-μm PP possess the most favorable lithium-ion diffusion properties. The higher D_{Li}+ of ZIF-8@8-μm PP than that of ZIF-8@25-μm PP implies the decreased thickness with less diffusion distance and tortuosity are conducive to lithium-ion diffusion.

2.4. Battery performance

The improved charge transfer properties of LSBs by incorporation of ZIF-8@8-μm PP are evident in its electrochemical impedance spectroscopy (EIS) profiles (Fig. S16). The EIS spectra were fitted using the equivalent circuit shown in Fig. S17, where R_e represents the bulk internal resistance of the electrolyte, separator, and electrode interfaces, R_{ct} is the charge transfer resistance, W_o denotes Warburg diffusion, and CPE represents a constant phase element[68]. The values of R_e and R_{ct} obtained from the fitting are summarized in Table S5. For fresh Li-S cells assembled with ZIF-8@8-μm PP, the smallest semi-circle loop in the high frequency region

indicates lowest charge transfer resistance, whilst the higher slope in the low frequency region suggests a trend towards an ideal ion diffusion behavior [69]. The open-circuit voltage profiles in Fig. 4(a) illustrate the self-discharge behavior of LSBs using different separators. The self-discharge rate follows the sequence: 8-μm PP > 25-μm PP > ZIF-8@ 25-μm PP> ZIF-8@8-μm PP. This sequence is consistent with the capacity decay rate observed in LSBs during the cycling and rate capability tests. In contrast to the rapid voltage drop with the pristine PP separator, the ZIF-8 modified separators slow down the self-discharge. This is achieved by inhibiting or suppressing crossover polysulfide diffusion, leading to a sustained stable plateau of 2.37 V.

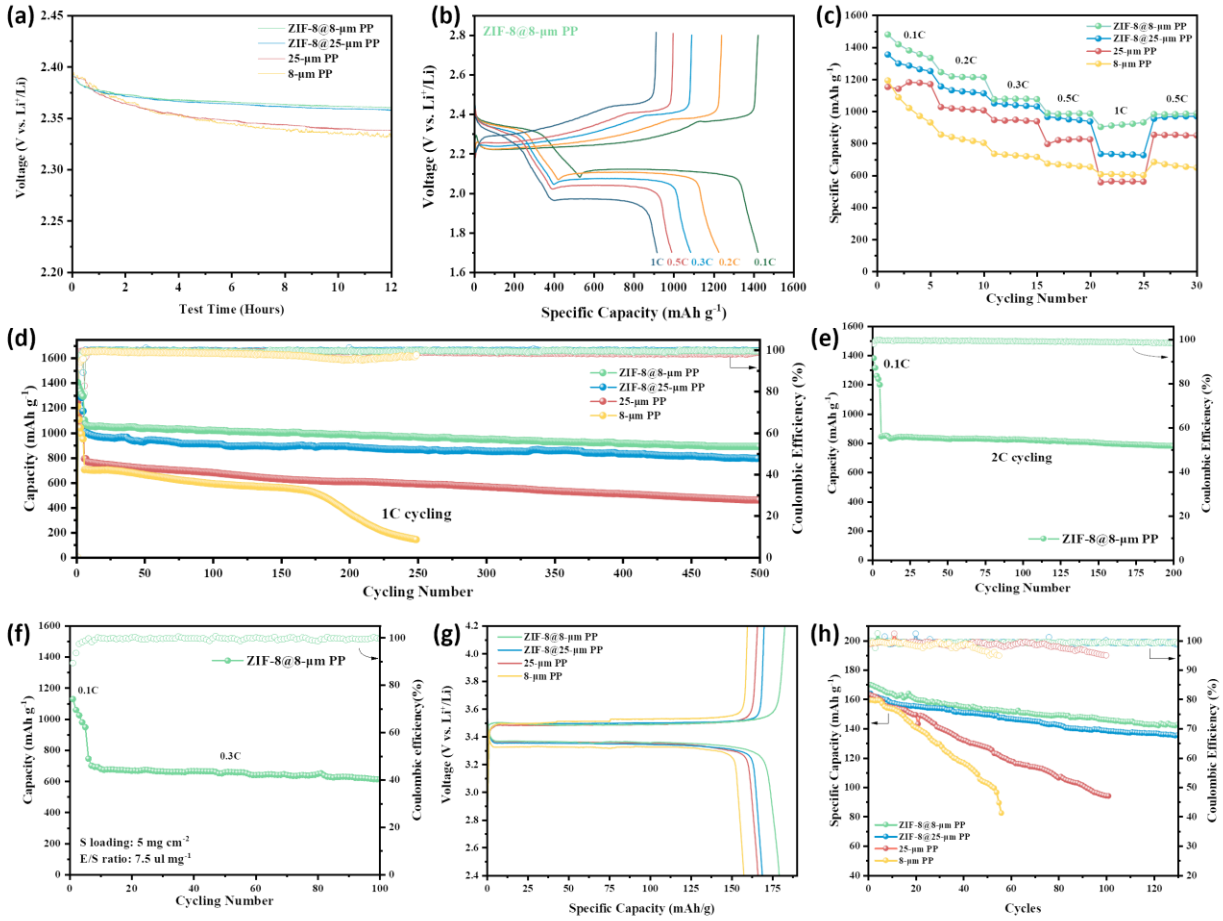

441

442 *Figure 4. (a) Open-circuit voltage (OCV) curves of Li-S cells assembled with different separators.*
443 *(b)Voltage charge/discharge profiles of Li-S cell coupled with ZIF-8@8-μm PP from 0.1 to 1 C.*
444 *(c) The rate capabilities demonstration of LSBs coupled with different separators. (d) Long-term*
445 *cyclic stability of LSBs coupled with different separators at 1C. (e) Long-term cyclic stability of*
446 *LSBs with ZIF-8@8-μm at 2C. (f) Long-term cyclic stability of LSBs with ZIF-8@8-μm at 0.3C*
447 *under high loading (5 mg cm^{-2}) and low E/S ratio (7.5 μL mg^{-1}) condition. (g) First cycle voltage-*
448 *capacity curves of LFP-Li cells with different separators at 0.1C. (h) Long-term cycling stability*
449 *of LFP-Li cells with different separators at 0.5C.*

The experiments collectively indicate that the application of ZIF-8@8-μm PP separator is highly beneficial for achieving high capacity and good cyclic stability in LSB performance at high current density. This is attributed to the ability of ZIF-8 to enhance wettability to the electrolyte, improve Li^+ ion conductivity and diffusion within the electrolyte, and effectively suppress the shuttle effect of LiPSs.

To assess the viability of the crack-free ZIF-8 functional layer modified PP separator in LSBs, a set of LSBs was assembled using different separators: pristine 8-μm PP, 25-μm PP, ZIF-8@25-μm PP and ZIF-8@8-μm PP. The assembled coin cells have a sulfur loading of 1.5 mg/cm^2 and E/S ratio of 15 μl/mg. The rate capability and cyclic performance of these cells were evaluated using galvanostatic charge/discharge measurement.

As depicted in Fig. 4(b)(c) and Fig. S18, batteries utilizing ZIF-8 modified separators exhibited an increasing rate capability, which became more pronounced with higher applied current density. Specifically, the batteries equipped with ZIF-8@8-μm PP separators delivered specific discharge capacities of 1480, 1250, 1090, 990, and 917 mAh·g^{-1} at current densities of 0.1C, 0.2C, 0.3C, 0.5C and 1C rate, respectively. Upon returning to a current density of 0.5C, the capacity remained stable at 968 mAh·g^{-1}. This superior rate capability can be attributed to the synergistic effect of ZIF-8 modification and ultrathin separator, which enhances wettability to the electrolyte and improved Li^+ conductivity and its transference number. In terms of LSBs cycled at a rate of 1C with different separators, the cells assembled with ZIF-8@8-μm demonstrated a retained capacity of ~891 mAh g^{-1} after 500 cycles from an initial capacity of ~1053 mAh g^{-1} (Fig. 4(d)). The capacity fading rate for each cycle is approximately 0.031%, which was the best among the four LSBs with different separators. In contrast, cells assembled with a commercial ultrathin 8-μm PP separator exhibited very fast capacity decay, experiencing sudden failure after only 160 cycles.

Moreover, when cycled at a high rate of 2C (Fig. 4(e)), Li-S cells assembled with ZIF-8@8-μm PP maintain a capacity of 785 mAh/g after 200 cycles. To meet the practical requirements of Li-S batteries, cells coupled with ZIF-8@8-μm PP were further tested with a higher sulfur loading of 5 mg/cm^2 and a lower E/S ratio of 7.5 μl/mg. As shown in Fig. 4(f), after being activated at 0.1C for 5 cycles, those cells assembled with ZIF-8@8-μm PP demonstrated outstanding cyclic stability at 0.3 C with a high capacity of 623 mAh/g after 100 cycles.

To further validate the application of the ZIF-8 modified separator in lithium metal batteries, these separators were tested in an LFP||Li cell configuration. The LFP-Li cells exhibited charge/discharge behavior with lowest polarization when using the ZIF-8@8-μm separator at both 0.1 and 0.5C rates. The LFP-Li cells achieved the highest first cycle capacity of 178 mAh/g at 0.1C and 167 mAh/g at 0.5C when using the ZIF-8@8-μm PP separator, as shown in Fig. 4(g) and Fig. S19. When tested over longer durations, cells with unmodified separators exhibited immediate capacity decay in the first few cycles, as shown in Fig. 4(h). In contrast, the ZIF-8 modified thin and thick separators maintained capacities of 138 mAh/g and 130 mAh/g, respectively, after 140 cycles. This indicates that ZIF-8 modification enables the functioning of a very thin 8-μm separator, potentially leading to the application of dendrite free lithium metal batteries.

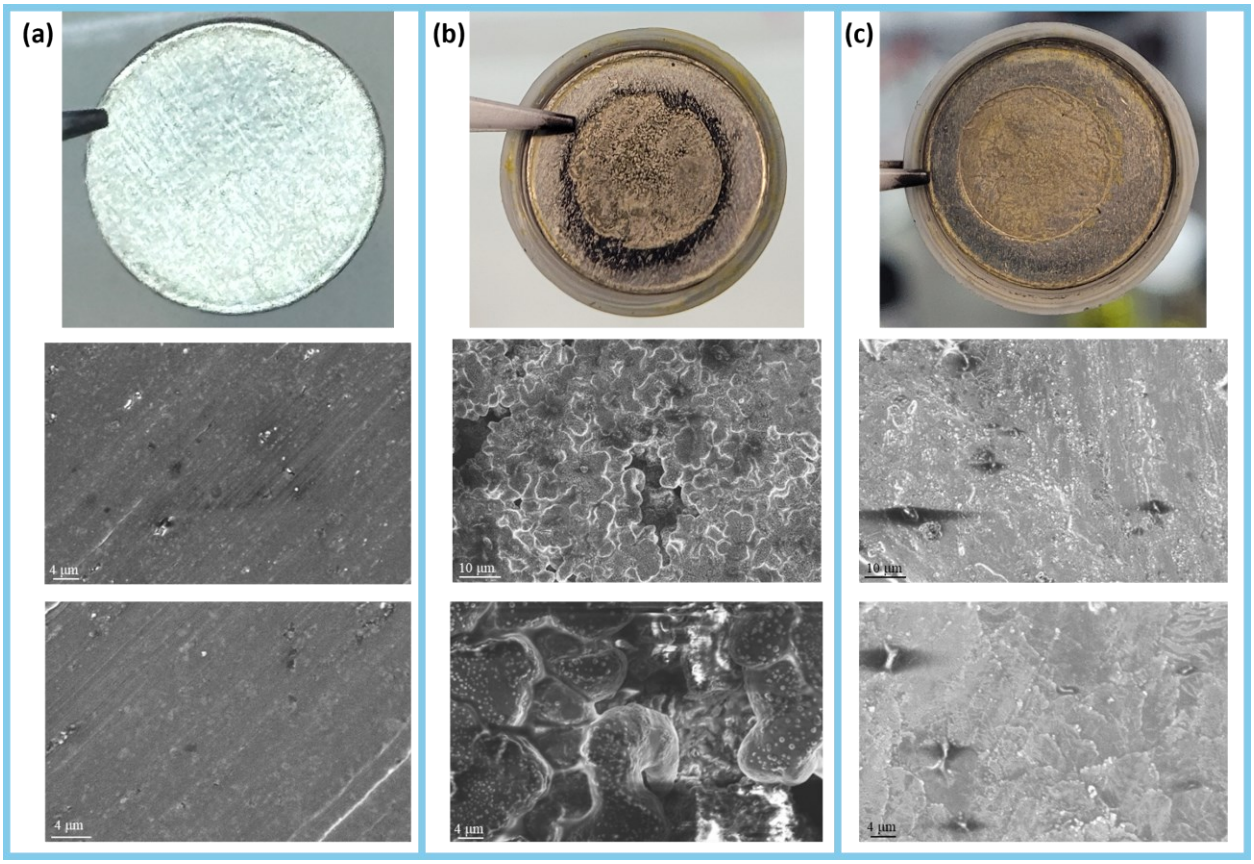

Figure 5. Digital images and corresponding surface morphology SEM images of the (a) pristine Li metal anode, (b) Li anode in cells coupled with 8-μm PP after 250 cycles and (c) Li anode in cells coupled with ZIF-8@8-μm PP after cycling 500 cycles.

We further conducted a postmortem examination of the cycled LSBs to inspect the effects of ZIF-8 coating on Li metal anodes. As shown in Fig. 5(a), the pristine Li anode exhibited a flat and glossy surface. However, the cycled Li anodes with 8-μm ultrathin PP displayed very rough and lumpy surfaces (Fig. 5(b)), caused by irreversible plating/stripping behavior and undesired corrosion reaction between Li and LiPSs. In contrast, after introducing ZIF-8 modification layer, the cycled Li anodes almost retained their original smooth morphology (Fig. 5(c)), indicating that

501 the ZIF-8@8-μm PP separator effectively confines LiPSs on the cathode side and regulates Li^+
502 flux and deposition. This finding was consistent with the previously discussed superior
503 electrochemical performance of ZIF-8@8-μm PP cells, in contrast to those low-performance
504 pristine PP cells.

505 SEM images of ZIF-8@8-μm PP before and after LSBs cycling were also captured to confirm
506 its cyclic stability. As shown in Fig. S20, the strong adhesion and retention of the ZIF-8 layer on
507 the surface of the 8-μm PP were observed after 500 cycles, with no significant changes. Compared
508 to the initial surface morphology depicted in Fig. S20(a) and (b), where ZIF-8 particles were
509 uniformly sharp, the particles post-cycling exhibit a slightly rough texture, and minor cracks are
510 visible on the previously continuous crack-free surface. The observed morphological changes
511 might be attributed to electrolyte etching, which gradually degrades the ZIF-8 surface, causing
512 roughness and structural alterations. Additionally, the volume expansion of the sulfur cathode
513 and lithium anode during cycling induces mechanical stress on the separator, leading to
514 deformation and crack formation in the ZIF-8 layer. Interactions with shuttled LiPSs during
515 cycling may also weaken the crystal structure over time. Despite these technical challenges during
516 cycling, the ZIF-8 ultra-thin layer maintains a well-defined structure with minimal degradation
517 after extended cycling, demonstrating the resilience of the ZIF-8@8-μm PP separators.

518

519 ## 3. Conclusion

520 In this study, we employed an aqueous cathodic deposition method to engineer a commercial
521 8-μm ultrathin PP separator with a compact ZIF-8 thin film. The resulting ZIF-8@8-μm PP
522 exhibits exceptional flexibility, electrolyte uptake capacity, wettability, and remarkable ability to

mitigate polysulfide shuttling due to its distinctive physiochemical properties. Moreover, higher ionic conductivity and transference number are achieved by the syngeneic effect of reduced separator thickness and the utilization of ZIF-8 as an ion/molecule sieve and Li^+ transport booster. Additionally, it promotes uniform lithium-ion flux and regulates Li deposition, thus enabling stable lithium plating/stripping behavior, evidenced by extended cycling life, lower polarization and higher Coulombic efficiency. With the ZIF-8 thin film modification, the LSBs utilizing the ZIF-8@8-μm PP separator demonstrate a superior initial capacity of 1480 mAh g^{-1}, along with a low capacity-degradation rate of 0.031% per cycle at 1C after 500 cycles. Similarly, Li||$LiFePO_4$ LMBs configured with the ZIF-8@8-μm PP also exhibit significantly enhanced electrochemical performance. Our results demonstrate that although the ultrathin 8-μm PP is not suitable as separator in batteries, the ultrathin ZIF-8@8-μm PP, with a micrometer crack-free ZIF-8 coating on 8-μm PP, has the mechanical strength and superior electrochemical properties to be applied as the separator in LSBs and LMBs.

4. **Experimental Section**

4.1. Preparation of the ZIF-8@PP separators by cathodic deposition

4.105 g 2-Methylimidazole (MIM) was initially dissolved in 50 ml DI water. Meanwhile, another aqueous solution was prepared by dissolving 0.183 g Zinc acetate dihydrate ($Zn(CH_3COO)_2 \cdot 2H_2O$) in another 10 ml DI water. The two solutions were mixed and stirred to prepare the ZIF-8 precursor solution for the cathodic electrodeposition. 8-μm ultrathin PP membranes were coated with gold via sputtering coating at 20 mA for 20 s. The gold-coated PP membranes, along with a graphite paper, were positioned parallel to each other with a separation distance of 1.5 cm and soaked in the ZIF-8 precursor solution. The current-driven cathodic electrodeposition process was performed for 60 min under a current density of 0.13 mA cm^{-2}.

546 The resultant membranes were thoroughly rinsed by DI water and methanol to remove the
547 residues after synthesis process. The obtained ZIF-8 coated 8-μm PP membrane was tailored and
548 named ZIF-8@8-μm PP separator. Similarly, ZIF-8@25-μm PP separators were prepared
549 through the same synthesis protocol while replacing the ultrathin 8-μm PP membranes by
550 conventional 25-μm PP membranes. The fabricated composite membranes were activated in
551 methanol and dried in vacuum oven at 80 ℃.

552 4.2. Material characterization

553 The morphologies of ZIF-8@PP separators and Li anodes before-and-after cycling were
554 observed by using Zeiss Auriga scanning electron microscope (SEM). The X-ray photoelectron
555 spectroscopy (XPS) spectra were measured by a Krator Axis Supra + apparatus using Al K-alpha
556 (1486.6 eV) as the excitation light source. Fourier-transform infrared (FT-IR) spectra were
557 recorded using a Nicolet 6700 FT-IR spectrometer to acquire the chemical bonding information.
558 The X-ray diffraction (XRD) patterns were obtained on Malvern PANalytical Aeris X-ray
559 Diffractometer with Cu Kα radiation (λ = 0.1541 nm) over the 2θ range of 10–80° with a scan
560 speed of 2° min^{-1} at room temperature. Differential scanning calorimetry (DSC) was performed
561 on a LABSYS EVO instrument by heating the samples from ambient temperature to 600 ℃ at a
562 rate of 20 ℃/min in Argon flow to verify the thermal stability. UV-Vis Spectrometer (Perkin
563 Lambda 950) was used to acquire UV-vis absorbance spectroscopy after polysulfide adsorption
564 tests.

565 4.3. Electrochemical measurements

566 To fabricate sulfur cathode, commercial Ketjenblack (KB) and sublimed sulfur (S) powder
567 were uniformly mixed by griding with a mass ratio of 3:7, then the mixed powder was heated at

155 °C under an argon atmosphere for 12 h to obtain KB/S composite by melt diffusion method. The slurry was prepared by mixing 80 wt% KB/S composite, 10 wt% acetylene black (AB) and 10 wt% polyvinylidene fluoride (PVDF) binder in N-methyl-2-pyrrolidinone (NMP) solvent and then slurry was coated on an aluminum foil through doctor-blade casting method. The as-prepared cathode with a sulfur loading of 1.5 mg/cm^2 was cut into disks (ϕ = 13 mm) after vacuum drying at 60 °C overnight. Li-S full cell was assembled in an argon-filled glove box with the sulfur cathode, 0.6 mm thick lithium foil (diameter of 20 mm) as the anode and ZIF-8@PP or pristine PP membranes as the separators. The ether-based electrolyte used in LSBs is made up of 1 M bis(trifluoromethanesulfonyl)imide lithium (LiTFSI) and 2 wt% Lithium nitrites ($LiNO_3$) in a mixed solvent of 1,2-dimethoxyethane (DME) and 1,3-dioxolane (DOL) with a volume ratio of 1:1. The E/S ratio is controlled to be 15 μl/mg for normal electrochemical tests. LSB cells with a high mass loading of 5 mg/cm^2 and a lower E/S ratio of 7.5 μl/mg were also assembled. The lithium stripping and plating cycling behavior is evaluated by assembling Li||Li symmetric cells and Li||Cu asymmetric cells coupled with different separators. The ether-based electrolyte (1 M LiTFSI with 2 wt% $LiNO_3$ in DOL/DME v/v=1:1) is also used in Li||Li and Li||Cu cells cycling tests. Li||$LiFePO_4$ batteries were assembled to test the applicability of different separators in another type of LMBs apart from LSBs. A commercial $LiFePO_4$/aluminum foil (single side coated, 12 mg cm^{-2}, MTI corporation) was used as the cathode, carbonated-based electrolyte comprising 1 M $LiPF_6$ in ethylene carbonate (EC), and ethyl methyl carbonate (EMC) as the electrolyte (MTI corporation), with the ratio of electrolyte and $LiFePO_4$ being ~ 10 μL/mg.

Galvanostatic charge-discharge cycling tests of the batteries between the voltage range of 1.7-2.8V were recorded with a LAND CT2001A battery tester. Cyclic voltammetry (CV) rate measurement and electrochemical impedance spectroscopy (EIS) were performed using a

591 Biologic SP-240 electrochemical workstation. CV tests were conducted within the voltage range
592 of 1.6-2.8 V (vs Li/Li+), at different scanning rates from 0.2 to 1 mV s^{-1}. EIS measurements were
593 carried out over a frequency range of 10^{5}–10^{-2} Hz with an amplitude of 5 mV.

594 **Acknowledgment**

595 This research was funded by National Science Foundation of U.S.A, grant number 2103582
596 and 2129983.

597 **Appendix A. Supplementary material**

598 Supplementary data to this article can be found online.

599

Reference

(1) Cheng, X.-B.; Zhang, R.; Zhao, C.-Z.; Zhang, Q. Toward safe lithium metal anode in rechargeable batteries: a review. *Chemical reviews* **2017**, *117*, 10403-10473.

(2) Yin, Y.-X.; Xin, S.; Guo, Y.-G.; Wan, L.-J. Lithium–Sulfur Batteries: Electrochemistry, Materials, and Prospects. *Angewandte Chemie International Edition* **2013**, *52*, 13186-13200.

(3) Li, S.; Lin, X.; Wang, S.; Zhu, H.; Fan, Z. Bacteria derived nanomaterials for lithium-based batteries. *Carbon* **2024**, *216*, 118564.

(4) Lin, D.; Liu, Y.; Cui, Y. Reviving the lithium metal anode for high-energy batteries. *Nature nanotechnology* **2017**, *12*, 194-206.

(5) Liu, T.; Hu, H.; Ding, X.; Yuan, H.; Jin, C.; Nai, J.; Liu, Y.; Wang, Y.; Wan, Y.; Tao, X. 12 years roadmap of the sulfur cathode for lithium sulfur batteries (2009–2020). *Energy Storage Materials* **2020**, *30*, 346-366.

(6) Rana, M.; Luo, B.; Kaiser, M. R.; Gentle, I.; Knibbe, R. The role of functional materials to produce high areal capacity lithium sulfur battery. *Journal of Energy Chemistry* **2020**, *42*, 195-209.

(7) Lin, X.; Li, W.; Pan, X.; Wang, S.; Fan, Z. Electrocatalytic and Conductive Vanadium Oxide on Carbonized Bacterial Cellulose Aerogel for the Sulfur Cathode in Li-S Batteries. *Batteries* **2023**, *9*, 14.

(8) Lin, X.; Li, W.; Nguyen, V.; Wang, S.; Yang, S.; Ma, L.; Du, Y.; Wang, B.; Fan, Z. Fe-single-atom catalyst nanocages linked by bacterial cellulose-derived carbon nanofiber aerogel for Li-S batteries. *Chemical Engineering Journal* **2023**, *477*, 146977.

(9) Gueon, D.; Ju, M.-Y.; Moon, J. H. Complete encapsulation of sulfur through interfacial energy control of sulfur solutions for high-performance Li–S batteries. *Proceedings of the National Academy of Sciences* **2020**, *117*, 12686-12692.

(10) Bai, P.; Li, J.; Brushett, F. R.; Bazant, M. Z. Transition of lithium growth mechanisms in liquid electrolytes. *Energy & Environmental Science* **2016**, *9*, 3221-3229.

(11) Wang, C.; Wang, A.; Ren, L.; Guan, X.; Wang, D.; Dong, A.; Zhang, C.; Li, G.; Luo, J. Controlling Li Ion Flux through Materials Innovation for Dendrite-Free Lithium Metal Anodes. *Advanced Functional Materials* **2019**, *29*, 1905940.

(12) Yu, X.; Feng, S.; Boyer, M. J.; Lee, M.; Ferrier, R. C.; Lynd, N. A.; Hwang, G. S.; Wang, G.; Swinnea, S.; Manthiram, A. Controlling the polysulfide diffusion in lithium-sulfur batteries with a polymer membrane with intrinsic nanoporosity. *Materials Today Energy* **2018**, *7*, 98-104.

(13) Deimede, V.; Elmasides, C. Separators for Lithium-Ion Batteries: A Review on the Production Processes and Recent Developments. *Energy Technology* **2015**, *3*, 453-468.

(14) Zhong, S.; Yuan, B.; Guang, Z.; Chen, D.; Li, Q.; Dong, L.; Ji, Y.; Dong, Y.; Han, J.; He, W. Recent progress in thin separators for upgraded lithium ion batteries. *Energy Storage Materials* **2021**, *41*, 805-841.

(15) Arora, P.; Zhang, Z. Battery separators. *Chemical reviews* **2004**, *104*, 4419-4462.

(16) Huang, Z.-D.; Yang, M.-T.; Qi, J.-Q.; Zhang, P.; Lei, L.; Du, Q.-C.; Bai, L.; Fu, H.; Yang, X.-S.; Liu, R.-Q.; Masese, T.; Zhang, H.; Ma, Y.-W. Mitigating the polysulfides “shuttling” with TiO2 nanowires/nanosheets hybrid modified separators for robust lithium-sulfur batteries. *Chemical Engineering Journal* **2020**, *387*, 124080.

(17) Zhang, Y.; Miao, L.; Ning, J.; Xiao, Z.; Hao, L.; Wang, B.; Zhi, L. A graphene-oxide-based thin coating on the separator: an efficient barrier towards high-stable lithium–sulfur batteries. *2D Materials* **2015**, *2*, 024013.

(18) Li, Z.; Hou, L.-P.; Zhang, X.-Q.; Li, B.-Q.; Huang, J.-Q.; Chen, C.-M.; Liu, Q.-B.; Xiang, R.; Zhang, Q. A Nafion protective layer for stabilizing lithium metal anodes in working lithium–sulfur batteries. *Battery Energy* **2022**, *1*, 20220006.

(19) Baranwal, R.; Lin, X.; Li, W.; Pan, X.; Wang, S.; Fan, Z. Biopolymer separators from polydopamine-functionalized bacterial cellulose for lithium-sulfur batteries. *Journal of Colloid and Interface Science* **2024**, *656*, 556-565.
(20) Zhou, C.; Li, Z.; Xu, X.; Mai, L. Metal-organic frameworks enable broad strategies for lithium-sulfur batteries. *National Science Review* **2021**, *8*.
(21) Bai, S.; Liu, X.; Zhu, K.; Wu, S.; Zhou, H. Metal–organic framework-based separator for lithium–sulfur batteries. *Nature Energy* **2016**, *1*, 16094.
(22) Chu, Z.; Gao, X.; Wang, C.; Wang, T.; Wang, G. Metal–organic frameworks as separators and electrolytes for lithium–sulfur batteries. *Journal of Materials Chemistry A* **2021**, *9*, 7301-7316.
(23) Zheng, Y.; Zheng, S.; Xue, H.; Pang, H. Metal–organic frameworks for lithium–sulfur batteries. *Journal of Materials Chemistry A* **2019**, *7*, 3469-3491.
(24) Zhang, C.; Shen, L.; Shen, J.; Liu, F.; Chen, G.; Tao, R.; Ma, S.; Peng, Y.; Lu, Y. Anion‐sorbent composite separators for high‐rate lithium‐ion batteries. *Advanced Materials* **2019**, *31*, 1808338.
(25) Liu, W.; Mi, Y.; Weng, Z.; Zhong, Y.; Wu, Z.; Wang, H. Functional metal–organic framework boosting lithium metal anode performance via chemical interactions. *Chemical Science* **2017**, *8*, 4285-4291.
(26) Lin, G.; Jia, K.; Bai, Z.; Liu, C.; Liu, S.; Huang, Y.; Liu, X. Metal‐Organic Framework Sandwiching Porous Super‐Engineering Polymeric Membranes as Anionphilic Separators for Dendrite‐free Lithium Metal Batteries. *Advanced Functional Materials* **2022**, *32*, 2207969.
(27) Bai, S.; Zhu, K.; Wu, S.; Wang, Y.; Yi, J.; Ishida, M.; Zhou, H. A long-life lithium–sulphur battery by integrating zinc–organic framework based separator. *Journal of Materials Chemistry A* **2016**, *4*, 16812-16817.
(28) Zhao, Y.; Wei, Y.; Lyu, L.; Hou, Q.; Caro, J.; Wang, H. Flexible Polypropylene-Supported ZIF-8 Membranes for Highly Efficient Propene/Propane Separation. *Journal of the American Chemical Society* **2020**, *142*, 20915-20919.
(29) Wang, Z.; Liu, L.; Li, Z.; Goyal, N.; Du, T.; He, J.; Li, G. K. Shaping of Metal–Organic Frameworks: A Review. *Energy & Fuels* **2022**, *36*, 2927-2944.
(30) Wei, R.; Chi, H.-Y.; Li, X.; Lu, D.; Wan, Y.; Yang, C.-W.; Lai, Z. Aqueously Cathodic Deposition of ZIF-8 Membranes for Superior Propylene/Propane Separation. *Advanced Functional Materials* **2020**, *30*, 1907089.
(31) Xie, S.; Zhou, Z.; Zhang, X.; Fransaer, J. Cathodic deposition of MOF films: mechanism and applications. *Chemical Society Reviews* **2023**, *52*, 4292-4312.
(32) Low, J. J.; Benin, A. I.; Jakubczak, P.; Abrahamian, J. F.; Faheem, S. A.; Willis, R. R. Virtual High Throughput Screening Confirmed Experimentally: Porous Coordination Polymer Hydration. *Journal of the American Chemical Society* **2009**, *131*, 15834-15842.
(33) Rangnekar, N.; Mittal, N.; Elyassi, B.; Caro, J.; Tsapatsis, M. Zeolite membranes – a review and comparison with MOFs. *Chemical Society Reviews* **2015**, *44*, 7128-7154.
(34) Chen, B.; Yang, Z.; Zhu, Y.; Xia, Y. Zeolitic imidazolate framework materials: recent progress in synthesis and applications. *Journal of Materials Chemistry A* **2014**, *2*, 16811-16831.
(35) Li, J.-R.; Sculley, J.; Zhou, H.-C. Metal–Organic Frameworks for Separations. *Chemical Reviews* **2012**, *112*, 869-932.
(36) Bux, H.; Liang, F.; Li, Y.; Cravillon, J.; Wiebcke, M.; Caro, J. Zeolitic Imidazolate Framework Membrane with Molecular Sieving Properties by Microwave-Assisted Solvothermal Synthesis. *Journal of the American Chemical Society* **2009**, *131*, 16000-16001.
(37) Bai, S.; Sun, Y.; Yi, J.; He, Y.; Qiao, Y.; Zhou, H. High-power Li-metal anode enabled by metal-organic framework modified electrolyte. *Joule* **2018**, *2*, 2117-2132.

(38) Jia, Z.; Hao, S.; Wen, J.; Li, S.; Peng, W.; Huang, R.; Xu, X. Electrochemical fabrication of metal–organic frameworks membranes and films: A review. *Microporous and Mesoporous Materials* **2020**, *305*, 110322.

(39) Zhou, S.; Wei, Y.; Li, L.; Duan, Y.; Hou, Q.; Zhang, L.; Ding, L. X.; Xue, J.; Wang, H.; Caro, J. Paralyzed membrane: Current-driven synthesis of a metal-organic framework with sharpened propene/propane separation. *Sci Adv* **2018**, *4*, eaau1393.

(40) Yadnum, S.; Roche, J.; Lebraud, E.; Négrier, P.; Garrigue, P.; Bradshaw, D.; Warakulwit, C.; Limtrakul, J.; Kuhn, A. Site-Selective Synthesis of Janus-type Metal-Organic Framework Composites. *Angewandte Chemie International Edition* **2014**, *53*, 4001-4005.

(41) Pan, Y.; Liu, Y.; Zeng, G.; Zhao, L.; Lai, Z. Rapid synthesis of zeolitic imidazolate framework-8 (ZIF-8) nanocrystals in an aqueous system. *Chemical Communications* **2011**, *47*, 2071-2073.

(42) Chang, Z.; Yang, H.; Pan, A.; He, P.; Zhou, H. An improved 9 micron thick separator for a 350 Wh/kg lithium metal rechargeable pouch cell. *Nature Communications* **2022**, *13*, 6788.

(43) Zhang, C.; Lively, R. P.; Zhang, K.; Johnson, J. R.; Karvan, O.; Koros, W. J. Unexpected Molecular Sieving Properties of Zeolitic Imidazolate Framework-8. *The Journal of Physical Chemistry Letters* **2012**, *3*, 2130-2134.

(44) Ariyoshi, S.; Hashimoto, S.; Ohnishi, S.; Negishi, S.; Mikami, H.; Hayashi, K.; Tanaka, S.; Hiroshiba, N. Broadband terahertz spectroscopy of cellulose nanofiber-reinforced polypropylenes. *Materials Science and Engineering: B* **2021**, *265*, 115000.

(45) Morris, W.; Stevens, C. J.; Taylor, R. E.; Dybowski, C.; Yaghi, O. M.; Garcia-Garibay, M. A. NMR and X-ray Study Revealing the Rigidity of Zeolitic Imidazolate Frameworks. *The Journal of Physical Chemistry C* **2012**, *116*, 13307-13312.

(46) Park, K. S.; Ni, Z.; Côté, A. P.; Choi, J. Y.; Huang, R.; Uribe-Romo, F. J.; Chae, H. K.; O'Keeffe, M.; Yaghi, O. M. Exceptional chemical and thermal stability of zeolitic imidazolate frameworks. *Proceedings of the National Academy of Sciences* **2006**, *103*, 10186-10191.

(47) Mphuthi, L. E.; Erasmus, E.; Langner, E. H. G. Metal Exchange of ZIF-8 and ZIF-67 Nanoparticles with Fe(II) for Enhanced Photocatalytic Performance. *ACS Omega* **2021**, *6*, 31632-31645.

(48) Dangwal, S.; Ronte, A.; Lin, H.; Liu, R.; Zhu, J.; Lee, J. S.; Gappa-Fahlenkamp, H.; Kim, S.-J. ZIF-8 membranes supported on silicalite-seeded substrates for propylene/propane separation. *Journal of Membrane Science* **2021**, *626*, 119165.

(49) Kravets, L. I.; Altynov, V. A.; Zagonenko, V. F.; Lizunov, N. E.; Satulu, V.; Mitu, B.; Dinescu, G. Composite Bilayer Polymer Membranes with Hydrophobic Layers. *Inorganic Materials: Applied Research* **2018**, *9*, 777-784.

(50) Luanwuthi, S.; Krittayavathananon, A.; Srimuk, P.; Sawangphruk, M. In situ synthesis of permselective zeolitic imidazolate framework-8/graphene oxide composites: rotating disk electrode and Langmuir adsorption isotherm. *RSC Advances* **2015**, *5*, 46617-46623.

(51) Minhas, F. T.; Memon, S.; Bhanger, M.; Iqbal, N.; Mujahid, M. J. A. s. s. Solvent resistant thin film composite nanofiltration membrane: characterization and permeation study. **2013**, *282*, 887-897.

(52) Rodriguez, R.; Palma, M. S.; Bhandari, D.; Tian, F. J. L. Electrodeposition of Ag/ZIF-8-Modified Membrane for Water Remediation. **2023**, *39*, 2291-2300.

(53) Bahar, E.; Ucar, N.; Onen, A.; Wang, Y.; Oksüz, M.; Ayaz, O.; Ucar, M.; Demir, A. Thermal and mechanical properties of polypropylene nanocomposite materials reinforced with cellulose nano whiskers. *Journal of Applied Polymer Science* **2012**, *125*, 2882-2889.

(54) Prasanna, K.; Kim, C.-S.; Lee, C. W. Effect of SiO2 coating on polyethylene separator with different stretching ratios for application in lithium ion batteries. *Materials Chemistry and Physics* **2014**, *146*, 545-550.

(55) Evans, J.; Vincent, C. A.; Bruce, P. G. Electrochemical measurement of transference numbers in polymer electrolytes. *Polymer* **1987**, *28*, 2324-2328.

(56) Zhang, S. S. Liquid electrolyte lithium/sulfur battery: Fundamental chemistry, problems, and solutions. *Journal of Power Sources* **2013**, *231*, 153-162.
(57) Rajput, N. N.; Murugesan, V.; Shin, Y.; Han, K. S.; Lau, K. C.; Chen, J.; Liu, J.; Curtiss, L. A.; Mueller, K. T.; Persson, K. A. Elucidating the Solvation Structure and Dynamics of Lithium Polysulfides Resulting from Competitive Salt and Solvent Interactions. *Chemistry of Materials* **2017**, *29*, 3375-3379.
(58) Zheng, J.; Tian, J.; Wu, D.; Gu, M.; Xu, W.; Wang, C.; Gao, F.; Engelhard, M. H.; Zhang, J.-G.; Liu, J.; Xiao, J. Lewis Acid–Base Interactions between Polysulfides and Metal Organic Framework in Lithium Sulfur Batteries. *Nano Letters* **2014**, *14*, 2345-2352.
(59) Song, J.; Gordin, M. L.; Xu, T.; Chen, S.; Yu, Z.; Sohn, H.; Lu, J.; Ren, Y.; Duan, Y.; Wang, D. Strong lithium polysulfide chemisorption on electroactive sites of nitrogen-doped carbon composites for high-performance lithium–sulfur battery cathodes. *Angewandte Chemie* **2015**, *127*, 4399-4403.
(60) Kang, X.; He, T.; Zou, R.; Niu, S.; Ma, Y.; Zhu, F.; Ran, F. Size Effect for Inhibiting Polysulfides Shuttle in Lithium-Sulfur Batteries. *Small* **2023**, 2306503.
(61) Ni, L.; Gu, J.; Jiang, X.; Xu, H.; Wu, Z.; Wu, Y.; Liu, Y.; Xie, J.; Wei, Y.; Diao, G. Polyoxometalate-Cyclodextrin-Based Cluster-Organic Supramolecular Framework for Polysulfide Conversion and Guest–Host Recognition in Lithium-sulfur Batteries. *Angewandte Chemie International Edition* **2023**, *62*, e202306528.
(62) Yang, Y.; Wang, W.; Li, L.; Li, B.; Zhang, J. Stable cycling of Li–S batteries by simultaneously suppressing Li-dendrite growth and polysulfide shuttling enabled by a bioinspired separator. *Journal of Materials Chemistry A* **2020**, *8*, 3692-3700.
(63) Zhu, Z.; Zeng, Y.; Pei, Z.; Luan, D.; Wang, X.; Lou, X. W. Bimetal-Organic Framework Nanoboxes Enable Accelerated Redox Kinetics and Polysulfide Trapping for Lithium-Sulfur Batteries. *Angewandte Chemie International Edition* **2023**, *62*, e202305828.
(64) Chen, K.-H.; Wood, K. N.; Kazyak, E.; LePage, W. S.; Davis, A. L.; Sanchez, A. J.; Dasgupta, N. P. Dead lithium: mass transport effects on voltage, capacity, and failure of lithium metal anodes. *Journal of Materials Chemistry A* **2017**, *5*, 11671-11681.
(65) Huang, X.; Wang, Z.; Knibbe, R.; Luo, B.; Ahad, S. A.; Sun, D.; Wang, L. Cyclic Voltammetry in Lithium–Sulfur Batteries—Challenges and Opportunities. *Energy Technology* **2019**, *7*, 1801001.
(66) Zhou, G.; Tian, H.; Jin, Y.; Tao, X.; Liu, B.; Zhang, R.; Seh, Z. W.; Zhuo, D.; Liu, Y.; Sun, J.; Zhao, J.; Zu, C.; Wu, D. S.; Zhang, Q.; Cui, Y. Catalytic oxidation of Li2S on the surface of metal sulfides for Li–S batteries. *Proceedings of the National Academy of Sciences* **2017**, *114*, 840-845.
(67) Huang, J.-Q.; Zhuang, T.-Z.; Zhang, Q.; Peng, H.-J.; Chen, C.-M.; Wei, F. Permselective Graphene Oxide Membrane for Highly Stable and Anti-Self-Discharge Lithium–Sulfur Batteries. *ACS Nano* **2015**, *9*, 3002-3011.
(68) Cañas, N. A.; Hirose, K.; Pascucci, B.; Wagner, N.; Friedrich, K. A.; Hiesgen, R. Investigations of lithium–sulfur batteries using electrochemical impedance spectroscopy. *Electrochimica Acta* **2013**, *97*, 42-51.
(69) Li, Z.; Sami, I.; Yang, J.; Li, J.; Kumar, R. V.; Chhowalla, M. Lithiated metallic molybdenum disulfide nanosheets for high-performance lithium–sulfur batteries. *Nature Energy* **2023**, *8*, 84-93.